Time-Frequency Features of 3-D Sound Propagation in Wedge-Shaped Oceanic Waveguides

Frédéric Sturm and Julien Bonnel, *Member, IEEE*

***Abstract*—This paper considers propagation of low-frequency broadband pulses in shallow water. It focuses on across-slope propagation in wedge-shaped oceanic waveguides and on single hydrophone receiving configurations. In a low-frequency shallow-water context, propagation is dispersive and usually described by modal theory. However, in the presence of a tilted bottom, propagation is also affected by 3-D effects (horizontal refractions). The paper shows that time-frequency analysis is a suitable tool to illustrate and understand 3-D propagation. It illustrates the pertinence of the time-frequency analysis of 3-D signal by proposing an algorithm to estimate the seabed slope using a single receiver. The method is benchmarked on numerical simulations, and successfully applied on small-scale experimental data.**

***Index Terms*—Normal mode propagation, time-frequency analysis, underwater acoustics, 3-D propagation.**

I. Introduction

In shallow-water and littoral environments, acoustic waves can propagate over relatively long distances, and the sound propagation is strongly influenced by the seabed properties. When considering low-frequency sources, the oceanic environment acts as a dispersive waveguide and sound propagation can be described appropriately by modal theory. The acoustic field can be separated into several components called modes, each of them propagating dispersively. In a single receiver context, an efficient tool to analyze modal dispersion is time-frequency (TF) analysis [1], [2]. It allows for modal filtering [3], [4], dispersion curve estimation [5], [6], and thus source localization [7] and geoacoustic inversion [8]–[10]. However, most dispersion-based studies consider only 2-D waveguides. In this paper, TF analysis is used to study the propagation of low-frequency broadband pulses in 3-D shallow-water waveguides, and more specifically in 3-D wedge-shaped environments. The objectives of this paper are twofold. First, the paper shows that TF analysis is a suitable tool to illustrate and understand across-slope propagation of broadband pulses in wedge-shaped waveguides. Second, the paper demonstrates that, as for 2-D cases, the TF dispersion of the modes contains information about the seabed. This phenomenon is illustrated with a simple algorithm allowing estimation of the seabed slope using a single receiver.

It has been demonstrated both numerically [11]–[15] and experimentally [16], [17] that acoustic propagation in wedge-shaped waveguides is affected by horizontal refraction. If source and receiver are far enough from each other, it can lead to remarkable 3-D effects. Correct prediction of these effects requires fully 3-D models and computation codes [18]. Among existing 3-D codes available in the underwater acoustics community, parabolic equation (PE)-based models are largely used [19]–[25], [15], [26]–[29]. In this paper, the 3-D PE code of [15] will be used. Its reasonable (at least at very low frequencies) computational cost allows calculations in four dimensions: three spatial dimensions and time. A Fourier synthesis approach is used to handle the time dependence of the acoustic signals. It is thus possible to simulate the propagation of broadband pulses, and to jointly address the problem of 3-D effects and TF dispersion.

Because of waveguide dispersion, the source signal is distorted during propagation. This dispersion is ambivalent. On the one hand, it tends to complicate the analysis of the received signal. On the other hand, if properly characterized, dispersion conveys information about the propagation medium and can be used as a tomographic tool. In this paper, it will be shown that TF dispersion of a broadband pulse propagated in a 3-D wedge-shaped waveguide is particularly affected by horizontal refraction effects. Because of the seabed slope, a given mode can be received twice on a single receiver, and the TF dispersions of both modal arrivals are greatly different from one another. As will be shown in this paper, the differences observed between the two arrivals of the same mode can be explained by modal ray considerations. The TF pattern of the received signal contains information on the 3-D configuration of the waveguide, and can thus be used at the core of an inversion process to estimate waveguide parameters. In particular, the paper will show that it is possible to estimate the seabed slope by matching the TF pattern of the received signal with simulated replicas.

The paper is organized as follows. Section II describes the 3-D propagation over a tilted bottom in a single-receiver context. First, it briefly describes the well-known results on across-slope propagation in wedge-shaped waveguides, and then introduces TF analysis and its advantages to analyze the 3-D effects. Section III shows how TF analysis can be used at the core of an algorithm to estimate the seabed slope. The estimation procedure is described in Section III-A and its sensitivity is studied in Section III-B. Small-scale experimental data are considered

Manuscript received November 24, 2014; revised July 09, 2015; accepted July 21, 2015. Date of publication December 17, 2015; date of current version July 12, 2016. The work of J. Bonnel was supported by the French Government Defence procurement agency (Direction Générale de l'Armement) under Project ANR-12-ASTR-0021-03 “MER CALME.”

Associate Editor: N. R. Chapman.

F. Sturm is with the Laboratoire de Mécanique des Fluides et d'Acoustique (UMR CNRS 5509), Université de Lyon, Ecole Centrale de Lyon, Ecully Cedex F-69134, France (e-mail: frederic.sturm@ec-lyon.fr).

J. Bonnel is with the Lab-STICC (UMR CNRS 6285), ENSTA Bretagne (Université Européenne de Bretagne), Brest Cedex 9 F-29806, France.

Digital Object Identifier 10.1109/JOE.2015.2461711

in Section IV. Finally, Section V provides some concluding remarks.

II. Three-Dimensional Propagation Analysis in a Single-Receiver Context

A. Time-Series Computation

We consider a 3-D wedge-shaped oceanic environment which consists of a lossless homogeneous water layer (sound speed: $c_w = 1488.12$ m/s, density: $\rho_w = 1$ g/cm^3) overlying a lossy half-space sediment bottom (sound speed: $c_{\text{sed}} = 1700$ m/s, density: $\rho_{\text{sed}} = 1.99$ g/cm^3, and absorption: 0.5 dB/λ). No shear energy is assumed in the sediment. An isotropic point source is situated at a depth of 9 m above the sloping bottom where the water depth is 44.5 m. The bottom slope is 4.5°. Simulated time series at a constant receiver depth of 8 m and at several distances in the across-slope direction, i.e., along the direction corresponding to the 44.5-m isobath, obtained by fully 3-D computations are plotted in Fig. 1. The source signal is a five-cycle pulse wave with a Gaussian-like envelope centered at frequency $f_c = 150$ Hz. The source pulse is displayed in the upper left subplot of Fig. 1. The numerical results were obtained using the 3-D PE-based model 3DWAPE [15] coupled with a Fourier synthesis technique to handle the time dependence of the source signal.

Before proceeding to the analysis of the time series displayed in Fig. 1, let us make some preliminary comments. Since the computation domain in the across-slope direction is range independent, it is seen by any 2-D model such as the classical Pekeris waveguide. In this specific direction, the waveguide leads to the existence of four distinct propagating modes at 150 Hz. Therefore, considering the broadband source pulse described above, the 2-D propagating signal would split up in four distinct wave packets, the dispersion of each individual modal wave packet increasing as the receiver moves out in range. In addition (see, for instance, [30]), for each propagating mode, the first arrivals would consist of high-frequency contributions, whereas the later arrivals would have a more low-frequency content (above the Airy phase).

The time series corresponding to the 3-D solutions, i.e., those displayed in Fig. 1, show a different modal structure. They give evidence of well-known 3-D effects for each propagating mode, e.g., multiple arrivals of each mode, being distinguishable at some ranges, then merging together and progressively disappearing as the receiver moves out across slope (mode shadow zone effect). The reader is referred to [15] for a more detailed description of the 3-D effects experienced by the propagating modes. Though less evident for the present wedge-like geometry than for the classical 3-D Acoustical Society of America (ASA) wedge benchmark (characterized by a 2.86° bottom slope), a closer examination of the 3-D received signals reveals that the frequency content of a given wave packet varies in range (compare, for instance, the wave packet associated to mode 3 at ranges of 1.5 and 2 km). This effect, which appears first for higher modes, is known as the range dependence of the cut-on frequency (or, equivalently, the frequency dependence of mode cutoff range) of a propagating mode [12], [13], [31]. Interestingly, we can observe (see, for instance, at a distance of

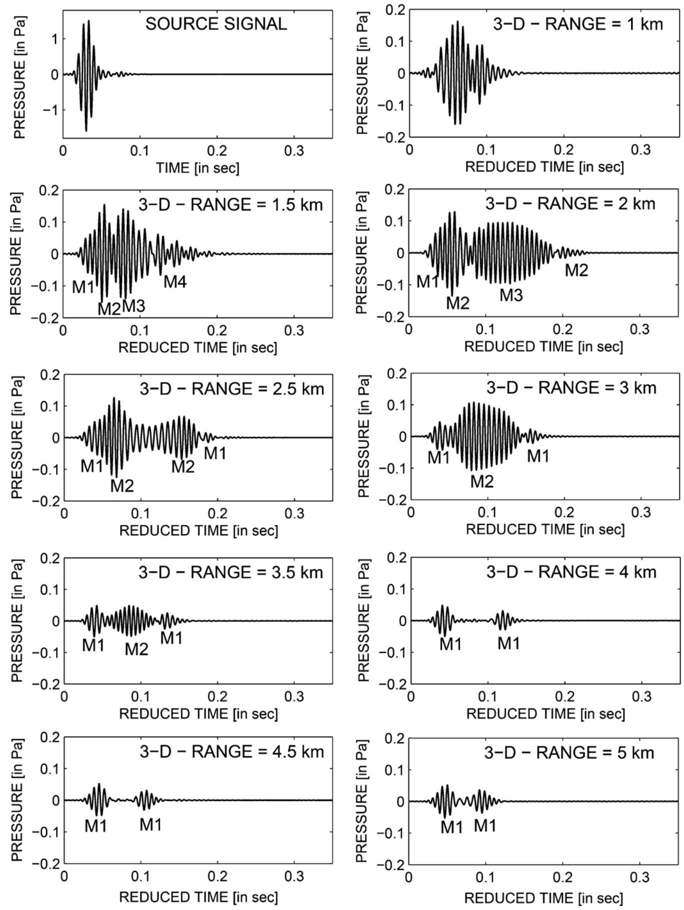

Fig. 1. Time series (receiver depth: 8 m) for a bottom slope of 4.5° at several distances (from 1 to 5 km) in the across-slope direction corresponding to fully 3-D computations using the 3-D PE code 3DWAPE. The simulated signals were scaled appropriately to compensate for cylindrical spreading. The source pulse is plotted in the upper left panel.

5 km), looking at the first 3-D modal arrival associated to mode 1, that high frequencies arrive before low frequencies (similar to the 2-D situation) whereas on the contrary, low frequencies arrive before high frequencies for the second 3-D arrival of mode 1. The same observation can be made when comparing the two adjacent 3-D modal arrivals of mode 2 at a distance of 2.5 km. As clearly shown hereafter, the TF analysis allows a much better visualization and understanding of this effect.

B. Time-Frequency Analysis

1) Spectrograms of 2-D and 3-D Signals: Let $s(t)$ denote the time-domain signal received on a single receiver after propagating in the wedge-shaped oceanic waveguide described above, computed using either 2-D calculation or fully 3-D calculation. The time-domain signal $s(t)$ can be brought into the TF domain using short time Fourier transform (STFT) as follows [1]:

$$\text{STFT}_s(t,f) = \int_{-\infty}^{\infty} s(\tau)\, w^*(\tau - t)\, e^{-i2\pi f t} d\tau \qquad (1)$$

where an asterisk denotes complex conjugation. In (1), $w(t)$ denotes a window function centered around zero. Spectrograms (SPs) of the received signals $s(t)$ are then given by

$$\text{SP}_s(t,f) = |\text{STFT}_s(t,f)|^2. \qquad (2)$$

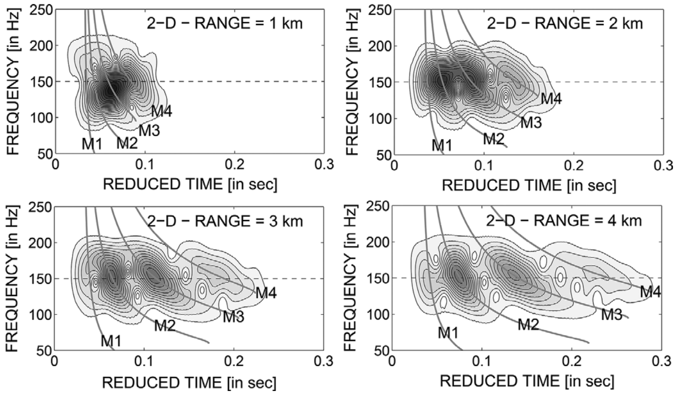

Fig. 2. Spectrograms of the simulated signals (receiver depth: 8 m) corresponding to 2-D computations at several across-slope distances (from 1 to 4 km). The gray curves superimposed on the SPs in each panel correspond to the 2-D theoretical dispersion curves of the propagating modes.

Fig. 2 shows the SPs of the received signals at a depth of 8 m, corresponding to 2-D computations, after propagation across slope for several ranges (from 1 to 4 km). The gray curves superimposed on the SPs in each panel correspond to the 2-D theoretical dispersion curves of the four propagating modes, given by $t_m(f) = r/c_{g,m}(f)$, $1 \leq m \leq 4$, where r denotes the source–receiver distance and $c_{g,m}(f)$ denotes the group speed of mode m at frequency f. Hence, $t_m(f)$ corresponds to the arrival time of mode m at frequency f. Note that, for each mode, the part of the theoretical dispersion curve corresponding to frequencies below the Airy phase is not displayed. The SPs of Fig. 2 follow the form of the dispersion curves, spread according to the window function used. We observe that at large ranges, modes are well separated in the TF domain. For relatively smaller source–receiver ranges, the modes tend to overlap (generating interferences) and become thus more hardly distinguishable in the TF domain (see [4] for a detailed study on modal TF separability). For a given mode m, the SPs confirm that the early arrivals of mode m consist of high-frequency contributions, whereas the late arrivals of mode m have a low-frequency content.

The SPs corresponding to fully 3-D computations are shown in Fig. 3 for several source–receiver distances (from 1 to 5 km with an increment of 0.5 km). As in Fig. 2, they correspond to receivers at a 8-m fixed depth situated in the across-slope direction. Several observations can be made. As in Fig. 2, the SPs enable the separation of the modal arrivals. However, unlike in 2-D, one mode can now have two distinct arrivals at some ranges and be missing at others. For instance, as in 2-D, there is one single arrival of mode 3 at both $r = 1$ km and $r = 1.5$ km; there are two arrivals of mode 3 at $r = 2$ km; mode 3 is absent for ranges larger than 2.5 km. Note that, if present, the second modal arrival can be well separated in time from the first modal arrival (see, for instance, at distances ranging from 2.5 to 5 km for mode 1) but can also be merged with the first modal arrival (see at $r = 3$ and 3.5 km for mode 2; see also at $r = 2$ km for mode 3). For each mode and for each source–receiver distance, the TF shape of the first modal arrival approximately follows the TF shape of the corresponding 2-D predictions shown in Fig. 2, with higher frequencies arriving first. The shape of the second modal arrival, when present, looks like the shape of the first one but is reversed in time, low frequencies arriving now first. We note that at short distances (e.g., at $r = 1$ km), each mode corresponds to an almost direct propagation between the source and the receiver and thus includes nearly no 3-D effects. As a consequence, its shape in the TF domain deviates only very slightly from the 2-D theoretical dispersion curve (plotted in gray for comparison). We observe, however, that even at $r = 1$ km, unlike the first three propagating modes, mode 4 deviates remarkably from its 2-D dispersion curve, indicating that the 3-D effects experienced by mode 4 cannot be neglected at $r = 1$ km. As the receiver moves out in range, we observe a now more pronounced deviation of the first arrival of each mode from the corresponding 2-D dispersion curve, this deviation appearing first for higher modes than for lower modes. We observe also that for a given propagating mode, as the receiver moves out in range, low frequencies disappear before high frequencies. This phenomenon, which is due to horizontal refraction effects, is precisely the range dependence of the cut-on frequency of a propagating mode, as discussed in Section II-A.

2) Mode Ray Analogies: All these observations can be explained using mode ray analogies as follows. First, recall that, when considering 3-D wedge-like oceanic waveguides, modes can be viewed, at a fixed frequency, as rays propagating along hyperbolic paths in the horizontal plane, being horizontally refracted toward regions of deeper water [36]. Modal ray paths can be easily determined using the method given in [22]. Let Γ_{m,ϕ_0} denote the modal ray path that corresponds to the mth mode and makes initially an angle $\phi_0 \in [-90°, 90°]$ with respect to the across-slope direction : $\phi_0 = 90°$ ($\phi_0 = -90°$) corresponds to an initial launch in the upslope direction (in the downslope direction) and $\phi_0 = 0°$ points across slope. For a wedge-shaped waveguide, and according to a Cartesian coordinate system centered on the source with the x-axis (resp., y-axis) corresponding to the across-slope (resp., upslope) direction, the water depth h depends on the y variable only and the modal ray path Γ_{m,ϕ_0} can be viewed as the graph of function $x \longmapsto y_{m,\phi_0}(x)$ satisfying the following first-order nonlinear ordinary differential equation:

$$\frac{dy}{dx} = \frac{\sqrt{1 - (c_m(y) \times \cos(\phi_0)/c_{r,m})^2}}{c_m(y) \times \cos(\phi_0)/c_{r,m}}, \qquad x \geq 0 \qquad (3)$$

and $y(x = 0) = 0$. In (3), c_m is the y-dependent phase velocity of the mth mode satisfying $c_w < c_m(y) < c_{\mathrm{sed}}$ and $c_m(y = 0) = c_{r,m}$, with $c_{r,m}$ the horizontal phase velocity of the mth mode at the source location. The value of $c_m(y)$ for any given y is numerically evaluated by solving the characteristic equation

$$\tan(\eta_m(y) \times h(y)) = -\frac{\rho_{\mathrm{sed}}}{\rho_w} \times \frac{\eta_m(y)}{\gamma_m(y)}$$

where $\eta_m(y)$ and $\gamma_m(y)$ are defined by

$$\eta_m(y) = \sqrt{(\omega/c_w)^2 - (\omega/c_m(y))^2}$$
$$\gamma_m(y) = \sqrt{(\omega/c_m(y))^2 - (\omega/c_{\mathrm{sed}})^2}$$

with $\omega = 2\pi f$. Modal rays, traveling first upslope (i.e., $\phi_0 > 0$), turn back downslope on condition that their grazing angles do not exceed the critical grazing angle, leading to a shadow zone

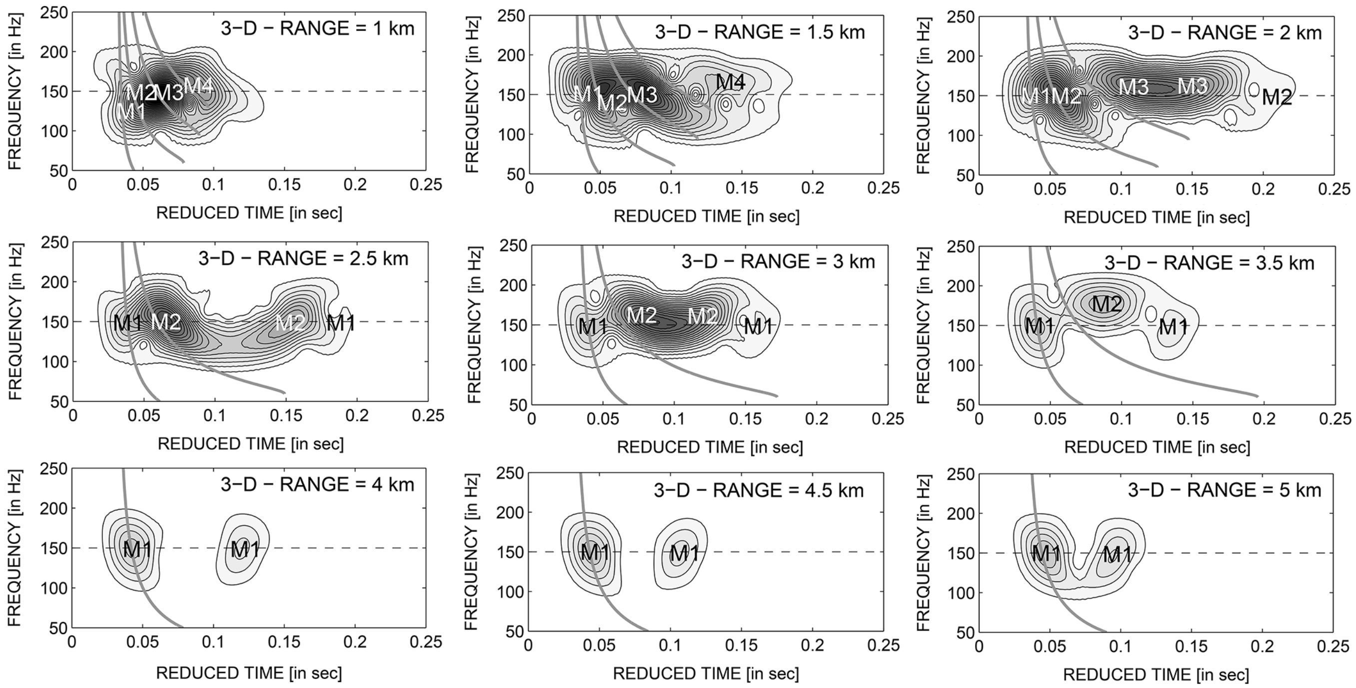

Fig. 3. Spectrograms of the simulated signals (receiver depth: 8 m) corresponding to fully 3-D computations at several across-slope distances (from 1 to 5 km). The gray curves superimposed on the SPs in each panel correspond to the 2-D theoretical dispersion curves of the propagating modes.

region in the across-slope direction at a sufficiently large distance from the source (the so-called mode cutoff range). The cutoff range of a given mode is shifted out in range with increasing frequency (see, for instance, [12]–[14], [31], and [32]). Considering a broadband source pulse, this means that the extinction of a given modal wave packet, instead of being abrupt, takes place in an extended region along the across-slope direction. This is what the SPs of Fig. 3 show for modes 4, 3, and 2; a larger maximum computation range would be required to see the same effect for mode 1. Assuming that, at a given frequency f, the receiver range is less than the cutoff range of mode m, and depending on its position along the across-slope direction, a receiver may see either one single arrival of mode m, or two distinct arrivals of the same mode m. In the latter case, the first mode arrival corresponds to a ray launched at a low horizontal angle $\phi_{0,1} > 0$ with respect to the across-slope direction, and the second to a ray launched at a higher horizontal angle $\phi_{0,2} > \phi_{0,1}$. Note that the first and second arrivals of the same mode are often referred to in the literature as "direct" arrival and "echo." The paths of these first and second eigenrays depend on frequency and source–receiver range. For example, the characteristics of the modal rays associated to mode 2 launched from the source and connected with a receiver in the across-slope direction are given in Table I for three frequencies ($f = 125$, 150, and 175 Hz) within the frequency band of the source pulse and for two source–receiver ranges ($r = 2.5$ and 3 km). The length and the travel time of a modal eigenray path, denoted, respectively, L_{ϕ_0} and t_{ϕ_0} in Table I, are obtained by integrating along the curve Γ_{m,ϕ_0} as follows:

$$L_{\phi_0} = \int_{\Gamma_{m,\phi_0}} ds, \quad t_{\phi_0} = \int_{\Gamma_{m,\phi_0}} \frac{ds}{c_{g,m}}$$

TABLE I
CHARACTERISTICS (FOR SEVERAL FREQUENCIES WITHIN THE FREQUENCY BAND OF THE SOURCE PULSE) OF THE MODAL RAYS ASSOCIATED TO MODE 2 LAUNCHED FROM THE SOURCE AND CONNECTED WITH A RECEIVER IN THE ACROSS-SLOPE DIRECTION. THE ANGLE ϕ_0 DENOTES THE INITIAL LAUNCH ANGLE ($\phi_0 = 90°$ POINTS UPSLOPE AND $\phi_0 = 0°$ POINTS ACROSS SLOPE) OF A MODAL EIGENRAY, L_{ϕ_0} DENOTES THE LENGTH OF A MODAL EIGENRAY PATH, AND t_{ϕ_0} DENOTES ITS TRAVEL TIME

	Receiver range: 2.5 km			Receiver range: 3 km		
f [Hz]	ϕ_0 [deg]	L_{ϕ_0} [m]	t_{ϕ_0} [sec]	ϕ_0 [deg]	L_{ϕ_0} [m]	t_{ϕ_0} [sec]
125	10.75	2 517.88	1.743	–	–	–
	15.60	2 543.21	1.773	–	–	–
150	5.90	2 504.87	1.715	9.85	3 018.42	2.075
	20.12	2 586.48	1.803	12.40	3 031.75	2.090
175	4.10	2 502.28	1.704	5.55	3 005.22	2.049
	21.70	2 610.49	1.814	16.40	3 066.15	2.117

where $c_{g,m}$ denotes the y-dependent group speed of mode m. Note that there are no data at 125 Hz in Table I for a receiver range of 3 km (which is beyond the cutoff range of mode 2 at 125 Hz).

Let us analyze first the frequency content of the first arrival (i.e., the "direct" arrival) of a mode. For a given mode m and a fixed source–receiver range, $\phi_{0,1}$ decreases as frequency increases. In other words, the higher frequency paths deviate less and less from the straight line connecting the source and the receiver as frequency increases (see Fig. 4). Therefore, the leading edge of the first arrival of mode m consists of high-frequency contributions and the trailing edge consists of low-frequency contributions. This is similar to what was observed for the single arrival of each propagating mode for the 2-D Pekeris waveguide (see the 2-D SPs shown in Fig. 2). For instance, for mode 2,

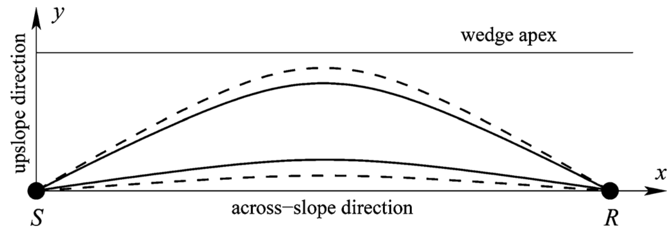

Fig. 4. Modal rays in the (horizontal) xy-plane associated to the same mode, launched from the source S and connected with a receiver R positioned along the across-slope direction, at two distinct frequencies f_1 (solid lines) and f_2 (dashed lines) with $f_2 > f_1$.

at a source–receiver range of 2.5 km, $\phi_{0,1}$ is equal to 10.75° (arrival time: 1.743 s) at 125 Hz and $\phi_{0,1}$ reduces to 4.1° (arrival time: 1.704 s) at 175 Hz. The 175-Hz eigenray arrives thus ≈0.039 s before the 125-Hz eigenray at 2.5 km. It is worth noting that, for each frequency, $\phi_{0,1}$ (i.e., the initial bending of the corresponding eigenray path), which is relatively low at small source–receiver ranges, increases as the receiver moves out in range (e.g., at 150 Hz, $\phi_{0,1} = 5.9°$ at $r = 2.5$ km and $\phi_{0,1} = 9.85°$ at $r = 3$ km). This explains why the shape of the first arrival of each mode deviates more and more in the TF domain from the corresponding theoretical 2-D dispersion curve as the receiver moves out in range.

Let us analyze now the frequency content of the second arrival (i.e., the "echo") of a mode. As illustrated in Fig. 4, for a given mode m and a fixed source–receiver range, $\phi_{0,2}$ now increases as frequency increases. The corresponding eigenray path penetrates farther into the shallower portion of the 3-D wedge-shaped waveguide as frequency increases. The low-frequency paths are thus shorter than the high-frequency paths, and low frequencies arrive now before high frequencies. The second arrival of a mode appears thus reversed in time in the TF domain. For instance, at a source–receiver range of 2.5 km, $\phi_{0,2} = 15.6°$ (arrival time: 1.773 s) at 125 Hz and $\phi_{0,2} = 21.7°$ (arrival time: 1.814 s) at 175 Hz for mode 2. Unlike the first arrival of mode 2, the 125-Hz eigenray for the second arrival of mode 2 arrives ≈0.041 s before the corresponding 175-Hz eigenray at $r = 2.5$ km.

III. Application

The main idea of this section is to demonstrate the pertinence of analyzing 3-D effects using TF analysis. For this purpose, we propose an algorithm allowing estimation of the seabed slope using simple TF analysis.

Classical single–receiver inversion schemes based on modal dispersion [8]–[10] in 2-D waveguides estimate dispersion curves $t_m(f)$ from the received signal, and compare them to parameter-dependent replicas $t_m(f, \alpha)$, where α is a set of parameters that characterize the oceanic environment. However, dispersion curve estimation requires dedicated TF methods, even in the classical 2-D case [2], [3], [5]. The proposed algorithm, although not based on dispersion curves, takes also advantage from the mode TF localization. It uses classical STFT and does not require other advanced TF processing.

A. Methodology

The algorithm compares the received signal $s_{\text{mes}}(t)$ with simulated replicas $s(t, \alpha)$, where α is the seabed slope used to compute the replicas. However, the matching function is computed in the TF domain, and focuses particularly on specific regions where modal energy is concentrated. More specifically, the algorithm finds energetic TF regions corresponding to a given slope α, and looks whether the corresponding TF regions of the received signal are energetic as well.

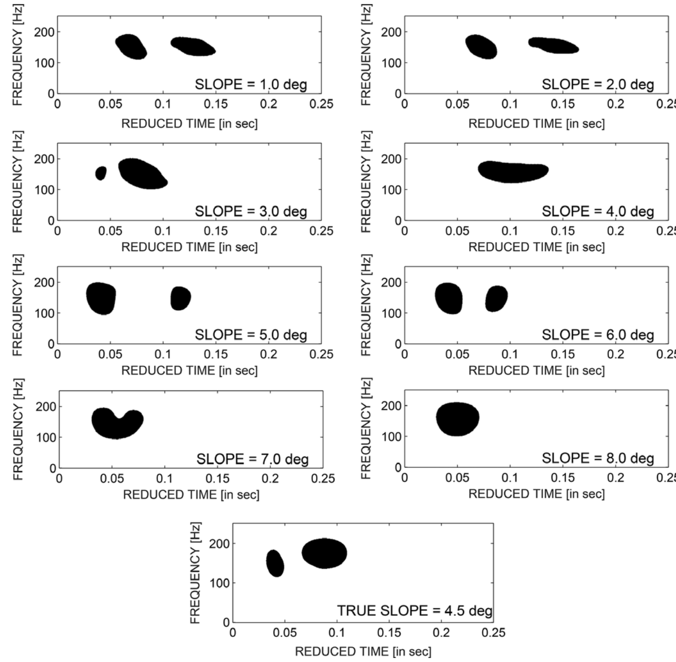

Fig. 5. Computed masks (black = 1, white = 0) for range $r = 3.5$ km and slope values from 1° to 8°.

To do so, time-domain replicas $s(t, \alpha)$ are computed using 3DWAPE and their $\text{SP}_s(t, f, \alpha)$ are computed using classical signal processing routines (see Section II). Then, a TF masking function $M(t, f, \alpha)$ is defined for each replica (for an example, see Fig. 5). The mask $M(t, f, \alpha)$ is a binary map of the TF domain with 1-values where modal energy is important and 0-values elsewhere. It is defined by comparing SP values with an energy threshold T_0 as follows:

$$M(t, f, \alpha) = \begin{cases} 1, & \text{if } \dfrac{\text{SP}_s(t, f, \alpha)}{\max \text{SP}_s(t, f, \alpha)} \geq T_0(\alpha) \\ 0, & \text{elsewhere.} \end{cases} \tag{4}$$

Note that the threshold value $0 < T_0(\alpha) < 1$ depends on α. Indeed, for estimation purpose, it is required that the mask energy (i.e., the number of 1-values) be constant for every replicas. Mathematically, the threshold value $T_0(\alpha)$ is defined for each α under the constraint $\int_t \int_f [M(t, f, \alpha)]^2 dt\, df = A$, where A is a constant. Specific A value is chosen so that the masks $M(t, f, \alpha)$ highlight the TF modal patterns.

To quantify the match between the received signal $s_{\text{mes}}(t)$ and the replicas $s(t, \alpha)$, a criterion function J is defined as the amount of measured TF energy integrated inside the masks

$$J(\alpha) = \int_t \int_f \text{SP}_{\text{mes}}(t, f)\, M(t, f, \alpha)\, dt\, df \tag{5}$$

where $\text{SP}_{\text{mes}}(t, f)$ is the SP of the received signal $s_{\text{mes}}(t)$. Note that $\int_t \int_f \text{SP}_{\text{mes}}(t, f) dt\, df$ corresponds to the received signal energy. The criterion $J(\alpha)$ is thus the energy of the received signal that is concentrated into a TF region defined by the mask $M(t, f, \alpha)$. If the replica $s(t, \alpha)$ matches the received signal $s_{\mathrm{mes}}(t)$, then the mask $M(t, f, \alpha)$ corresponds to a highly energetic TF region. Consequently, the estimated slope $\widehat{\alpha}$ is the one that maximizes J

$$\widehat{\alpha} = \underset{\alpha}{\operatorname{argmax}}[J(\alpha)]. \quad (6)$$

Estimation of $\widehat{\alpha}$ thus requires the maximization of the criterion J. As the criterion function J is mono-dimensional, its maximization can be obtained using a simple grid search. Note that the masking process, given by (5) and (6), is similar to what was done by Gervaise *et al.* [33] in the context of single-receiver geoacoustic inversion using broadband ship noise.

B. Simulated Data

In this section, the slope estimation algorithm described in Section III-A is applied on simulated data. The criterion function $J(\alpha)$ will be maximized using grid search for α between 1° (lower bound) and 8° (upper bound) with a discretization step of 0.25°. Considered simulated signals are the ones that have been used to compute the SPs in Fig. 3. This section is restricted to ranges from 1 to 3.5 km, as it allows meaningful comparisons with the available experimental data presented in Section IV. To study its sensitivity, the estimation algorithm is applied on noise-free simulated signals. The criterion J is computed for every source–receiver ranges (from 1 to 3.5 km with 0.5-km steps). The inversion is run for three sets of threshold value: $T_1(\alpha)$, $T_2(\alpha)$, and $T_3(\alpha)$, so that three different criteria J_1, J_2, and J_3 are computed for each range.

As explained in Section III-A, the threshold is adapted for each replica so that the area covered by the mask $M(t, f, \alpha)$ stays constant during the inversion. Here, the threshold sets $T_1(\alpha)$, $T_2(\alpha)$, and $T_3(\alpha)$ are chosen so that:

- for a given threshold set $T_i(\alpha)$, the areas covered by the corresponding masks are constant;
- the mask areas corresponding to $T_2(\alpha)$ are 50% smaller than for $T_1(\alpha)$;
- the mask areas corresponding to $T_3(\alpha)$ are 50% bigger than for $T_1(\alpha)$;
- the three average threshold values denoted $\widetilde{T_1}$, $\widetilde{T_2}$, and $\widetilde{T_3}$ are equal to 0.48, 0.65, and 0.37, respectively.

The inversion results are presented in Fig. 6. One can observe that, whatever the source–receiver range, the inversion is not sensitive to the threshold value. At the shortest range (1 km), the criterion is nearly flat, which means that, at that range, the estimation sensitivity is very poor, and one can assume that slope estimation will not be possible in a real case scenario. This can be explained by looking at the corresponding SP displayed in the upper left panel of Fig. 3. As discussed in Section II-B, at that distance, the differences between the 3-D modal patterns of modes 1–3 and the corresponding 2-D dispersion curves are barely visible, which indicates that there is nearly no 3-D effects for modes 1–3. Although mode 4 appears to be more affected by 3-D effects, it overlaps in the TF domain with mode 3. It is thus difficult to benefit from its TF dispersion, and as a consequence to estimate the seabed slope.

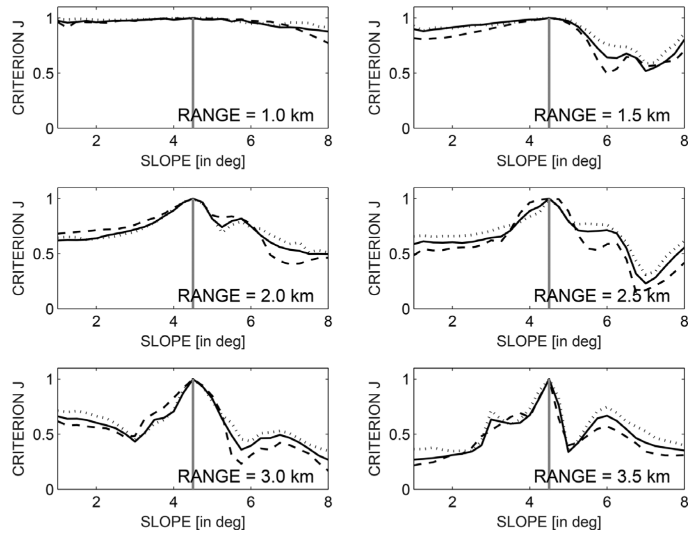

Fig. 6. Normalized criteria for several source–receiver ranges and for several threshold values. On each panel, J_1 is given by the solid line, J_2 is given by the dashed line, and J_3 is given by the dotted line; the vertical gray line indicates the true value (4.5°) of the bottom slope.

When increasing the source–receiver range: 1) the modal TF separation tends to increase; 2) the TF shapes of the "direct" arrivals differ more and more from the corresponding 2-D dispersion curves; and 3) the 3-D "echoes" appear. As a result, estimation gains in sensitivity: the criterion main maximum becomes more and more identifiable. It is clear that this phenomenon will stop if one goes farther in range than the shadow zone of mode 1 (Section II-A).

Another interesting (but penalizing) property of criterion J is that it possesses several ambiguity sidelobes, which can be attributed to the masking process. As an example, let us consider the 3.5-km case. At that distance, the computed criterion J exhibits two ambiguity sidelobes corresponding to slope values of 3° and 6° (see Fig. 6, $r = 3.5$ km). Indeed, looking at the corresponding computed masks (see Fig. 5, slopes 3° and 6°), one can observe that they possess 1-values at locations in the TF domain where there is actually energy in the received signal (displayed in Fig. 3, $r = 3.5$ km). More specifically, considering only the 6° replica, the mask focuses on the two arrivals ("direct" arrival at time $t \simeq 0.04$ s and its "echo" at $t \simeq 0.08$ s) of mode 1 (see Fig. 5, slope 6°). Once applied on the received signal (see Fig. 6, $r = 3.5$ km), the first part of the mask ($t \simeq 0.04$ s) integrates the energy corresponding to the "direct" arrival of mode 1, while the second part of the mask ($t \simeq 0.08$ s) integrates the energy corresponding to the merger of both "direct" arrival and "echo" of mode 2. Consequently, although the replica does not correspond to the measured signal, the mask still integrates modal energy. This phenomenon generates a sidelobe in the criterion J. The same kind of argument can be retained to justify the presence of other sidelobes. Note that the presence of nonnegligible sidelobes at some ranges is a penalizing factor for the estimation process and additional tests performed to assess the estimation algorithm under different signal-to-noise ratio (SNR) conditions showed that it can lead to wrong slope estimation under low SNR conditions (results not shown here). However, Section IV

TABLE II
SLOPE ESTIMATION RESULT WHEN MISMATCH IN THE SEABED SOUND SPEED IS CONSIDERED. THE TRUE SEABED SOUND SPEED IS 1700 m/s WHILE THE REPLICA ARE COMPUTED WITH 1625, 1650, 1725, 1750, AND 1775 m/s. THE TRUE SLOPE IS 4.5°

Slope [deg]		Replica seabed sound speed [m/s]					
		1625	1650	1675	1725	1750	1775
Range [km]	1	1	1	3.75	5.25	5.25	5.25
	1.5	3.75	4	4.5	4.5	4.75	5
	2	3.75	4	4.25	4.5	4.5	4.5
	2.5	4.25	4.25	4.5	4.5	4.5	4.5
	3	4.5	4.5	4.5	4.5	4.5	4.5
	3.5	4.5	4.5	4.5	4.5	4.5	4.5

will show that the algorithm is robust enough to provide good slope estimation on experimental data.

Before going further with experimental data, it is interesting to test the robustness of the inversion method when some environmental parameters are not known perfectly. In particular, it may be unrealistic to assume that the seabed geoacoustic parameters are known exactly. As a consequence, we consider environmental mismatch for the seabed sound speed $c_{\rm sed}$. The whole method is run with replica computed with $c_{\rm sed}$ equal to 1625, 1650, 1675, 1725, 1750, and 1775 m/s, while the true $c_{\rm sed}$ is equal to 1700 m/s. The corresponding slope estimation results are presented in Table II (note that the true slope is 4.5°). For a reasonable seabed mismatch (± 50 m/s), the slope estimation is nearly unaffected, except at very short ranges (i.e., ranges less than 1 km). When mismatch increases, the slope estimation result deteriorates. Except at short ranges, the estimated slope stays in the order of magnitude.

IV. EXPERIMENTAL DATA

To demonstrate the practical capability of the estimation algorithm, it is applied on small-scale experimental data. The scaled experiments were conducted in July 2007 in the large indoor tank of the LMA-CNRS laboratory in Marseille, France. The following paragraphs summarize important experimental features while a detailed description of the experimental protocol can be found in [34].

The tank consists in a thin layer of fresh water overlying a thick layer of calibrated river sand. Its dimensions are 10-m length, 3-m width, and 1-m depth. A sloping bottom geometry with the wedge apex oriented lengthwise over the entire length of the tank was created using a rake inclined at $\simeq$4.5°. The water depth at the source, measured using a high-frequency transducer, is $\simeq$45 mm. The water sound speed, deduced from the water temperature [35], is 1488.12 m/s. The geoacoustic parameters of the sandy bottom were measured on separate sand samples and refined using *in situ* acoustic experiments. Their values are: sound speed 1700$\pm$50 m/s, density 1.99$\pm$0.01 g/cm^3, and attenuation 0.5$\pm$0.1 dB/λ.

The source signal is a five-cycle pulse with Gaussian envelope with 0.04-ms duration. The source spectrum is centered at 150 kHz with a 100-kHz bandwidth. The source depth is $\simeq$9 mm and the receiver depth is $\simeq$8 mm. The propagation track is in the across-slope direction. The SPs corresponding to the experimental signals are displayed in Fig. 7 for source–receiver distances from 1 to 3.5 m with 50-cm steps. Experimental signals possess an excellent SNR.

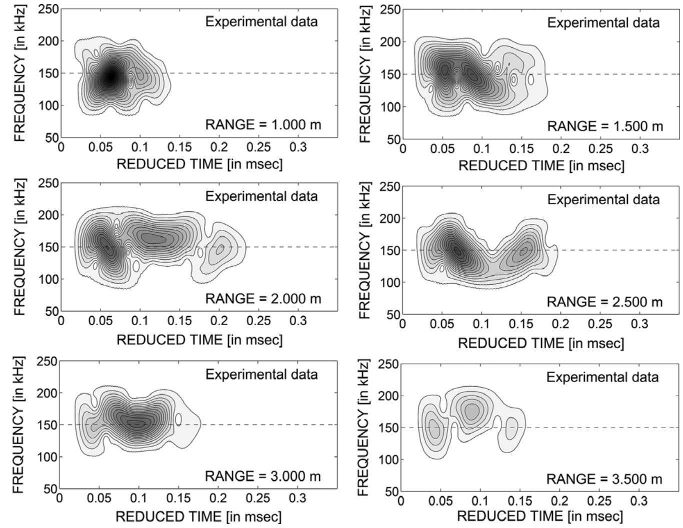

Fig. 7. Spectrograms of the experimental received signals collected during the tank experiment at several across-slope distances (from 1 to 3.5 m).

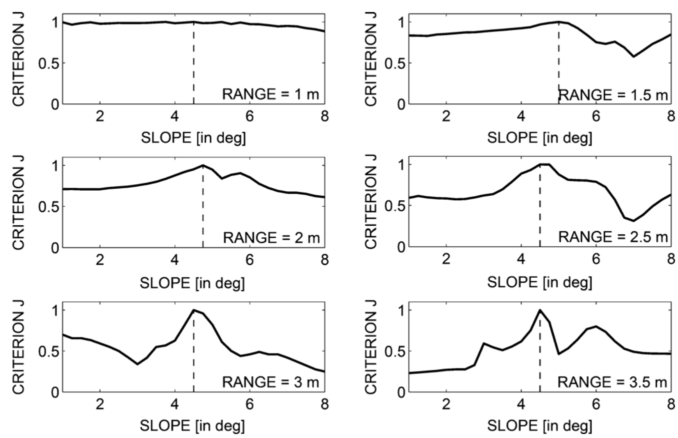

Fig. 8. Normalized criterion J for the experimental data for several source–receiver ranges. On each panel, the vertical dashed line indicates the estimated value of the slope: $\widehat{\alpha} = 4.5°$ except for range 1.5 m ($\widehat{\alpha} = 5.0°$) and 2 m ($\widehat{\alpha} = 4.75°$). Note that the experimental bottom slope α is approximately 4.5°.

The whole small-scale experiment mimics the long-range shallow-water propagation scenario described in Section II with a scale factor of 1000:1. Note that, as shown meticulously in [34], the experimental signals, whose SPs are shown in Fig. 7, compare very well with the simulated signals presented in Fig. 3.

The slope of the tilted bottom in the tank was estimated considering each of the experimental signals whose SPs are shown in Fig. 7. Estimated values of the slope are $\widehat{\alpha} = 4.5°$ for every ranges, with the exception of range 1.5 m ($\widehat{\alpha} = 5.0°$) and range 2 m ($\widehat{\alpha} = 4.75°$). Corresponding criteria J, presented in Fig. 8, compare favorably with the simulated ones (shown in Fig. 6).

These results are satisfactory and prove estimation efficiency for experimental data with good SNR. Note that, although the experimental protocol was well calibrated, all experimental parameters are known up to a (often unknown) precision. The good estimation results obtained considering experimental data show that the estimation algorithm is robust to relatively small theory error (model mismatch).

V. Conclusion

In this paper, 3-D propagation in wedge-shaped oceanic waveguides was considered. It was shown that TF analysis is a suitable tool to analyze across-slope propagation and, in particular, it provides interesting insights on the modal dispersion of the 3-D signals. It was shown also that the TF domain is particularly well suited to better understand horizontal refraction phenomena. Indeed, at certain ranges, a given mode can possess two distinct arrivals: the first arrival often referred to as "direct," and the second arrival called "echo." The "direct" arrival has a TF dispersion very similar to the TF dispersion in classical 2-D shallow-water waveguides, with high frequencies arriving before low frequencies. On the contrary, the "echo" (when present) always appears time reversed; its TF dispersion consists now in low frequencies arriving before high frequencies. This phenomenon has been explained using mode ray analogy. Because the "echo" high-frequency content can go further upslope than the "echo" lower frequencies, it travels a longer way between the source and the receiver, and finally arrives after lower frequencies.

This interesting phenomenon creates characteristic patterns in the SPs of the received signals. These patterns carry information about the 3-D varying properties of the waveguide, and can be used as the input of an estimation scheme to estimate parameters that characterize the 3-D varying oceanic environment. In this paper, which focuses on oceanic waveguides with wedge-shaped geometries, we proposed an estimation algorithm which allows estimating the bottom slope using a single receiver. It is based on comparisons of SPs of the received signal with SPs of simulated replica, by focusing on particular parts of the TF domain where modal dispersion is important. The sensitivity of the estimation algorithm was studied on simulated data. An experimental validation was performed on small-scale data recorded in an ultrasonic tank. While the experimental data have a really good SNR, some experimental parameters are not known with a good precision. The estimation algorithm nonetheless allows an accurate estimation of the sandy bottom slope.

Although this paper focuses on slope estimation, the proposed technique may be used also to infer other environmental parameters, such as source range and/or seabed geoacoustic properties. Because the TF modal pattern highly depends on range, the proposed method should allow accurate source localization. The method, however, is not highly sensitive to seabed sound speed; it is likely that it would not be effective to perform geoacoustic inversion. However, it is well known that classical TF-based modal inversions allow accurate geoacoustic inversion [8]–[10]. These methods are based on modal TF dispersion curves, while the method proposed in this paper is based on modal TF masks. The dispersion curves are the exact localization of the modes in the TF domain while the masks are the global positions of the modal energy in the TF domain. It is thus natural that the methods in [8]–[10] are more sensitive to small modifications of the modal TF pattern (such as those created by small variations of the seabed sound speed or density). A meaningful point demonstrated in this paper is that the TF patterns of the modes are highly impacted by 3-D propagation effects. However, existing modal inversion schemes based on TF dispersion curves never consider potential 3-D effects. Future work should consider such effects and their impact on the estimated geoacoustic parameters.

References

[1] F. Hlawatsch and G. Boudreaux-Bartels, "Linear and quadratic time-frequency signal representations," *IEEE Signal Process. Mag.*, vol. 9, no. 2, pp. 21–67, Apr. 1992.

[2] J. Bonnel, G. Le Touzé, B. Nicolas, and J. Mars, "Physics-based time-frequency representations for underwater acoustics: Power class utilization with waveguide-invariant approximation," *IEEE Signal Process. Mag.*, vol. 30, no. 6, pp. 120–129, Nov. 2013.

[3] G. Le Touzé, B. Nicolas, J. Mars, and J. Lacoume, "Matched representations and filters for guided waves," *IEEE Trans. Signal Process.*, vol. 57, no. 5, pp. 1783–1795, May 2009.

[4] J. Bonnel, C. Gervaise, P. Roux, B. Nicolas, and J. Mars, "Modal depth function estimation using time-frequency analysis," *J. Acoust. Soc. Amer.*, vol. 130, pp. 61–71, 2011.

[5] J. Hong, K. Sun, and Y. Kim, "Dispersion-based short-time Fourier transform applied to dispersive wave analysis," *J. Acoust. Soc. Amer.*, vol. 117, pp. 2949–2960, 2005.

[6] J. Bonnel, B. Nicolas, J. Mars, and S. Walker, "Estimation of modal group velocities with a single receiver for geoacoustic inversion in shallow water," *J. Acoust. Soc. Amer.*, vol. 128, pp. 719–727, 2010.

[7] J. Bonnel, A. M. Thode, S. B. Blackwell, K. Kim, and A. M. Macrander, "Range estimation of bowhead whale (Balaena mysticetus) calls in the Arctic using a single hydrophone," *J. Acoust. Soc. Amer.*, vol. 136, pp. 145–155, 2014.

[8] G. Potty, J. Miller, J. Lynch, and K. Smith, "Tomographic inversion for sediment parameters in shallow water," *J. Acoust. Soc. Amer.*, vol. 108, pp. 973–986, 2000.

[9] S. Rajan and K. Becker, "Inversion for range-dependent sediment compressional-wave-speed profiles from modal dispersion data," *IEEE J. Ocean. Eng.*, vol. 35, no. 1, pp. 43–58, Jan. 2010.

[10] J. Bonnel, S. E. Dosso, and N. R. Chapman, "Bayesian geoacoustic inversion of single hydrophone light bulb data using warping dispersion analysis," *J. Acoust. Soc. Amer.*, vol. 134, pp. 120–130, 2014.

[11] D. E. Weston, "Horizontal refraction in a three-dimensional medium of variable stratification," *Proc. Phys. Soc.*, vol. 78, pp. 46–52, 1961.

[12] C. H. Harrison, "Acoustic shadow zones in the horizontal plane," *J. Acoust. Soc. Amer.*, vol. 65, pp. 56–61, 1979.

[13] M. J. Buckingham, "Theory of three-dimensional acoustic propagation in a wedgelike ocean with a penetrable bottom," *J. Acoust. Soc. Amer.*, vol. 82, pp. 198–210, 1987.

[14] E. K. Westwood, "Broadband modeling of the three-dimensional penetrable wedge," *J. Acoust. Soc. Amer.*, vol. 92, pp. 2212–2222, 1992.

[15] F. Sturm, "Numerical study of broadband sound pulse propagation in three-dimensional oceanic waveguides," *J. Acoust. Soc. Amer.*, vol. 117, pp. 1058–1079, 2005.

[16] R. Doolittle, A. Tolstoy, and M. Buckingham, "Experimental confirmation of horizontal refraction of CW acoustic radiation from a point source in a wedge-shaped ocean environment," *J. Acoust. Soc. Amer.*, vol. 83, pp. 2117–2125, 1988.

[17] A. Korakas, F. Sturm, J.-P. Sessarego, and D. Ferrand, "Scaled model experiment of long-range across-slope pulse propagation in a penetrable wedge," *J. Acoust. Soc. Amer.*, vol. 126, pp. EL22–EL27, 2009.

[18] A. Tolstoy, "3-D propagation issues and models," *J. Comput. Acoust.*, vol. 4, pp. 243–271, 1996.

[19] D. Lee, A. Pierce, and E. Shang, "Parabolic equation development in the twentieth century," *J. Comput. Acoust.*, vol. 8, pp. 527–637, 2000.

[20] M. Collins and S. Ching-Bing, "A three-dimensional parabolic equation model that includes the effects of rough boundaries," *J. Acoust. Soc. Amer.*, vol. 87, pp. 1104–1109, 1990.

[21] D. Lee, G. Botseas, and W. Siegmann, "Examination of three-dimensional effects using a propagation model with azimuth-coupling capability (FOR3D)," *J. Acoust. Soc. Amer.*, vol. 91, pp. 3192–3202, 1992.

[22] J. A. Fawcett, "Modeling three-dimensional propagation in an oceanic wedge using parabolic equation methods," *J. Acoust. Soc. Amer.*, vol. 93, pp. 2627–2632, 1993.

[23] K. Smith, "A three-dimensional propagation algorithm using finite azimuthal aperture," *J. Acoust. Soc. Amer.*, vol. 106, pp. 3231–3239, 1999.

[24] C. F. Chen, Y.-T. Lin, and D. Lee, "A three-dimensional azimuthal wide-angle model," *J. Comput. Acoust.*, vol. 7, pp. 269–288, 1999.

[25] G. H. Brooke, D. J. Thomson, and G. R. Ebbeson, "PECan: A canadian parabolic equation model for underwater sound propagation," *J. Comput. Acoust.*, vol. 9, pp. 69–100, 2001.

[26] M. E. Austin and N. R. Chapman, "The use of tessellation in three-dimensional parabolic equation modeling," *J. Comput. Acoust.*, vol. 19, pp. 221–239, 2011.

[27] Y.-T. Lin and T. Duda, "A higher-order split-step Fourier parabolic-equation sound propagation solution scheme," *J. Acoust. Soc. Amer.*, vol. 132, pp. EL61–EL67, 2012.

[28] Y.-T. Lin, J. Collis, and T. Duda, "A three-dimensional parabolic equation model of sound propagation using higher-order operator splitting and padé approximants," *J. Acoust. Soc. Amer.*, vol. 132, pp. EL364–EL370, 2012.

[29] Y.-T. Lin, T. Duda, and A. Newhall, "Three-dimensional sound propagation models using the parabolic-equation approximation and the split-step Fourier method," *J. Comput. Acoust.*, vol. 21, 2013, 1250018.

[30] F. Jensen, W. Kuperman, M. Porter, and H. Schmidt, *Computational Ocean Acoustics*, ser. Modern Acoustics and Signal Processing. New York, NY, USA: Springer-Verlag, 2011, ch. 5.

[31] S. A. L. Glegg, G. B. Deane, and I. G. House, "Comparison between theory and model scale measurements of three-dimensional sound propagation in a shear supporting penetrable wedge," *J. Acoust. Soc. Amer.*, vol. 94, pp. 2334–2342, 1993.

[32] S. A. L. Glegg and J. R. Yoon, "Experimental measurements of three-dimensional propagation in a wedge-shaped ocean with pressure-release boundary conditions," *J. Acoust. Soc. Amer.*, vol. 87, pp. 101–105, 1990.

[33] C. Gervaise, B. Kinda, J. Bonnel, Y. Stefan, and S. Vallez, "Passive geoacoustic inversion with a single hydrophone using broadband ship noise," *J. Acoust. Soc. Amer.*, vol. 131, pp. 1999–2010, 2012.

[34] F. Sturm and A. Korakas, "Comparisons of laboratory scale measurements of three-dimensional acoustic propagation with solutions by a parabolic equation model," *J. Acoust. Soc. Amer.*, vol. 133, pp. 108–118, 2013.

[35] N. Bilaniuk and G. S. K. Wong, "Speed of sound in pure water as a function of temperature," *J. Acoust. Soc. Amer.*, vol. 93, pp. 1609–1612, 1993.

[36] H. Weinberg and R. Burridge, "Horizontal ray-theory for ocean acoustics," *J. Acoust. Soc. Amer.*, vol. 55, pp. 63–79, 1974.

Frédéric Sturm was born in Toulon, France, in 1969. He received the M.Sc. degree in applied mathematics from the University of Aix-Marseille I, Marseille, France, in 1993, the Ph.D. degree in acoustics from the University of Toulon, Toulon, France, in 1997, and the accreditation to supervise research degree (abbreviated HDR in French) in sciences from the University of Lyon, France, in 2011.

Since 1999, he has been an Assistant Professor at the INSA Engineering School, Lyon, France, where he teaches mathematics and numerical analysis in the internationally oriented section ASINSA. He is the coauthor of several mathematics textbooks. He is involved in the research activities of the Acoustics and Fluid Mechanics Laboratory (LMFA, UMR CNRS 5509, ECL, UCBL1, INSA Lyon). His present research interests include acoustic propagation and inversion problems in 3-D oceanic environments. His research combines theoretical, numerical, and experimental studies.

Julien Bonnel (S'08–M'11) received the Ph.D. degree in signal processing from Grenoble Institut National Polytechnique (Grenoble INP), Grenoble, France, in 2010.

Since 2010, he has been an Assistant Professor at Lab-STICC (UMR 6285), ENSTA Bretagne, Brest, France. His research in signal processing and underwater acoustics includes time-frequency analysis, source detection/localization, geoacoustic inversion, acoustical tomography, passive acoustic monitoring, and bioacoustics.

Prof. Bonnel is a member of the Acoustical Society of America.